Microkinetic modeling of lean NOx trap chemistry under reducing conditions

Richard S. Larson [a,*], Josh A. Pihl [b], V. Kalyana Chakravarthy [b],
Todd J. Toops [b], C. Stuart Daw [b]

[a] *Sandia National Laboratories, P.O. Box 969, Livermore, CA 94551-0969, USA*
[b] *Oak Ridge National Laboratory, Fuels, Engines and Emissions Research Center, 2360 Cherahala Boulevard, Knoxville, TN 37932-1563, USA*

Available online 12 February 2008

Abstract

An elementary surface reaction mechanism describing the chemistry on the precious metal sites of a lean NOx trap is developed. Kinetic parameters for all of the reactions are found by fitting reactor simulations to an extensive experimental database. Each experiment involves the steady flow of a reactant mixture through a monolith core sample under conditions designed to minimize NOx storage; in each case, the temperature is slowly ramped over a wide range in order to provide a large amount of data. A reaction mechanism involving 28 elementary steps is able to reproduce the results for 21 separate experimental runs quite well. The thermodynamic consistency of the mechanism is assured through the imposition of constraints on a well-defined subset of the rate parameters. It is found that the mechanism can occasionally lead to multiple steady-state behavior due to the existence of parallel reduction pathways. DRIFTS experiments corroborate some of the key mechanistic steps.
© 2007 Elsevier B.V. All rights reserved.

Keywords: Lean NOx trap (LNT); NOx storage reduction (NSR); Regeneration; Ammonia formation

1. Introduction

Control of NOx emissions from diesel or lean burn gasoline engines is a considerable technical barrier that must be overcome if the fuel efficiency advantages of these engines are to be fully realized. Unfortunately, three-way catalysts designed for stoichiometric engines will not remove NOx under lean conditions. NOx storage-reduction catalysts (also known as lean NOx traps or LNTs) and urea-based selective catalytic reduction (SCR) are currently the leading candidate technologies under consideration for lean NOx control.

In NOx traps, NOx is removed from the exhaust and stored over alkali- or alkaline-earth metal oxides in the form of nitrites and nitrates during normal lean operation. Periodically, brief reducing conditions are imposed on the NOx trap (either from rich engine operation or direct post-engine fuel injection) to generate reductants such as CO, H_2, and hydrocarbons. These reductants stimulate NOx release/desorption (by decomposing nitrites and nitrates) and then catalytically reduce the released NOx. Generally the desired reduction product is N_2, but it is also possible to form byproducts such as N_2O and NH_3. Both of these compounds are pollutants if released to the atmosphere, so their production typically must be minimized. However, in some instances (such as hybrid LNT/SCR systems), NH_3 formation is desirable. Regardless of the desired product mix, NOx trap regeneration involves a direct fuel penalty, so it is important to utilize the reductants as efficiently as possible. For all of these reasons, it is critical to understand the chemical reactions and operating conditions driving LNT regeneration product selectivity.

Much has been published on NOx traps since they were first reported by Toyota in the mid-1990s [1]. Most of the early work focused on determining the mechanism of the NOx storage process and improving sulfur tolerance [2], and there was limited emphasis on the regeneration process. Several authors considered the effectiveness of various reductant species at releasing and reducing the nitrites and nitrates stored on the catalyst surface, and they found that reactivity decreased in the order $H_2 > CO > C_3H_6 > C_3H_8$, with H_2 showing far better performance at low temperatures and with aged samples [3–5].

---

* Corresponding author. Tel.: +1 925 294 3008; fax: +1 925 294 3870.
   E-mail address: rslarso@sandia.gov (R.S. Larson).

Product selectivity was not generally considered to be an issue, as no one had reported substantial formation of products other than N_2. Early reaction mechanisms typically assumed complete conversion to N_2 [6], with a few including steps leading to formation of N_2O [7].

Regeneration product speciation received more attention after Lesage and co-workers reported the formation of substantial quantities of NH_3 during NOx trap regeneration using either H_2 or CO as the reductant [8,9]. According to their mass spectrometry traces, NH_3 formation commenced as N_2 production stopped and reductant breakthrough occurred. Using *in situ* FTIR, they observed Ba and Al isocyanates on the Pt–Rh/Ba/Al$_2$O$_3$ catalyst (likely due to spillover from the precious metal sites) during regeneration with CO, and they proposed isocyanate hydrolysis as the pathway to NH_3 formation when CO was the reductant.

While investigating Ba loading effects in Pt/Ba/Al$_2$O$_3$ catalysts, Castoldi et al. [10] observed NH_3 formation when the Ba loading was at least 16%. Increasing the Ba loading generated more NH_3. Like Lesage et al., Castoldi and co-workers observed a sequential regeneration process that initially showed high selectivity toward N_2, with a shift to NH_3 formation upon reductant breakthrough.

In their study of the effects of different reducing agents on a Pt/Ba/Al$_2$O$_3$ catalyst, Abdulhamid et al. [5] observed significant NH_3 formation with H_2 as the reductant. The NH_3 formation decreased at lower temperatures. No NH_3 was observed with CO or hydrocarbon reductants, though the experiments were run under dry conditions. They observed N_2O formation with CO as the reductant, and the selectivity to N_2O increased at lower temperatures.

Observations of regeneration byproducts are not limited to synthetic exhaust mixtures and model catalysts. Parks et al. demonstrated formation of NH_3 and N_2O during cyclic operation of a fully formulated LNT catalyst operated in engine exhaust [11]. Motivated by these observations of NH_3 and N_2O formation in the literature and in our own laboratory, we conducted a detailed experimental investigation of regeneration product selectivity [12].

The exact mechanism for the first step in the regeneration of a NOx trap – release of NOx from the nitrates and nitrites on the catalyst surface – is still a subject of debate. Possibilities include spillover of reductant species from precious metal sites to reduce the stored nitrates [13]; release driven by a shift in the gas/surface equilibrium due to a sudden drop in O_2 and NOx in the gas phase (and likely involving competition between surface nitrates, carbonates, and hydroxides) [14]; and thermal decomposition of nitrates due to the exotherm generated by reactions between the reductant and residual oxygen in the gas feed [15] or on the catalyst surface. It is likely that all three of these processes will occur in operating lean NOx traps, with the dominant mechanism determined by the specific operating conditions. Regardless of the release mechanism, we expect that NOx trap regeneration product speciation will be dominated by the selectivity of the reduction reactions occurring on the precious metal components of the NOx trap catalyst. We therefore focused the present investigation on the

second step in the regeneration process, the reduction of released NOx to N_2 and other products at precious metal sites [12].

To isolate the precious metal reduction reactions from the NOx storage and release process, we conducted our experiments with a simultaneous flow of NOx species and reductants over the NOx trap catalyst. In the presence of both H_2O and CO_2, we found that the steady-state selectivity trends were independent of the NOx species (NO or NO_2) and the reductant (H_2 or CO) fed to the catalyst. At low temperatures (below about 200°C), the reduction reactions yielded a mix of N_2, NH_3, and N_2O. At higher temperatures, the product distribution was determined by the ratio of NOx to reductant. Under feeds that were stoichiometric for N_2 formation, the reactions were highly selective to N_2. In the presence of excess reductant, NH_3 was the major reduction product.

In an attempt to understand the temporal evolution of products typically seen during regeneration, we also looked at reactions that could lead to the destruction of NH_3 and N_2O formed inside the catalyst [12]. We observed that N_2O is readily reduced to N_2 by both H_2 and CO. We also found that NH_3 can react with O_2 to form a mixture of products, including N_2, N_2O, and even NO, while the reaction between NH_3 and NO is highly selective to N_2.

Based on these steady-state experimental results, we developed a conceptual model of the actual regeneration process that explains the observed transient product selectivity trends [12]. The model is predicated on the existence of a reductant front that progresses through the catalyst bed more slowly than the gas flow. This front divides the catalyst bed into three sections: the section in contact with the front, the portion upstream of the front, and the portion downstream of the front. At the reductant front, the precious metal sites are covered by a mixture of adsorbed NOx and reductant, with the ratio of the two dependent on the relative rates of the release and reduction processes. If the ratio of reductant to NOx is close to stoichiometric for N_2 formation, then the reduction reactions generate primarily N_2. If there is excess reductant, then NH_3 formation dominates. If NOx species dominate the surface, then N_2O or NO is released.

While the above model predicts that a substantial portion of the stored NOx is released at the reductant front, we also propose that there are typically some ''slow'' storage sites (perhaps those that are far removed from precious metal particles) that decompose after the reductant front has passed. Any NOx released behind the front encounters a precious metal surface covered by reductant species and is reduced to NH_3. This NH_3 is convected downstream where it eventually encounters an unregenerated surface that is still covered by stored NOx and oxygen species. Our steady-flow experiments suggest that this NH_3 is oxidized by these species to form N_2, N_2O, or even NOx. Thus, even though NH_3 is formed in the upstream portions of the catalyst throughout the regeneration, the secondary oxidation reactions prevent it from slipping out the back of the catalyst until after most of the surface has been reduced.

The above conceptual model of transient NOx trap reduction fits quite well with other recently published work on

regeneration product selectivity. Nova and coworkers recently reported a study on the effects of temperature, reductant concentration, and NOx loading on product selectivity during regeneration of a Pt/Ba/Al$_2$O$_3$ catalyst with H$_2$ [16]. As usual, NH$_3$ production was only observed after H$_2$ breakthrough in all of their experiments. Interestingly, the NH$_3$ formation increased as the amount of NOx loaded during the storage phase was increased. At higher loadings, more NOx is stored at slow sites (those not associated with Pt particles), resulting in more NOx released behind the reductant front where the high reductant concentrations reduce the NOx to NH$_3$. In their conclusion, the authors suggest that "ammonia formation is related to nitrate species stored on Ba sites far from Pt and/or to a high H/N ratio on the catalyst surface," which is in agreement with the conceptual model discussed above.

Another recent paper from Cumaranatunge et al. [17] presented a picture of the NOx trap regeneration process that is similar to what we have discussed, in that it invokes formation and subsequent oxidation of NH$_3$ to explain the NH$_3$ slip behavior. They performed an experiment that showed that NH$_3$ is just as effective at regenerating a NOx trap as is H$_2$ at 300 °C under dry and CO$_2$-free conditions. They also conducted a series of steady-state reduction experiments at 300 °C where they measured the product selectivity as a function of NO to reductant ratio. Their results showed trends similar to ours: the NO + H$_2$ reaction was highly selective to N$_2$ at a 1:1 ratio but formed primarily NH$_3$ at higher reductant levels, and the NO + NH$_3$ reaction was quite selective to N$_2$ at NO:NH$_3$ ratios of less than 1.5.

Szailer et al. conducted an *in situ* FTIR/mass spectrometry investigation on regeneration of a Pt/Ba/Al$_2$O$_3$ NOx trap catalyst with H$_2$ and CO as reductants [18]. In agreement with previous studies, they found H$_2$ to be a much more efficient reductant than CO. They also observed formation of isocyanates on oxide components of the catalyst when CO was the reductant. In the presence of water, these isocyanates were readily hydrolyzed to form NH$_3$, which subsequently reacted with stored nitrates to form N$_2$.

In the present paper, we propose a microkinetic mechanism for the reactions occurring over the precious metal components of a NOx trap catalyst regenerated with H$_2$ or CO. The mechanism is intended to serve as the foundation for a quantitative transient model of the regeneration process that predicts the trends in product selectivity we have observed in our experiments. Kinetic parameters for the mechanism were determined by fitting simulation results to the experimental data reported in a previous paper [12].

The modeling work described here contains a substantially improved version of the microkinetic mechanism that we proposed earlier [19]. More recently Xu et al. [20] reported on a somewhat similar study of NO reduction by H$_2$. They presented a mechanism that involves a subset of the reactions reported here, with some additional simplifications being made to ease the computations. Our work differs from theirs in several important ways. Most notably, the present paper considers the additional reductant CO, accounts for the presence of CO$_2$ and H$_2$O in the feed, includes secondary reactions of the initial reduction products NH$_3$ and N$_2$O, employs strictly mass-action kinetics, uses a reactor model that accurately accounts for axial gradients, and rigorously enforces thermodynamic consistency throughout. On the other hand, our paper places less emphasis on gas-phase mass transfer resistance, although we provide evidence that this issue is of minor importance in the experiments considered here. We also do not employ an energy balance, since the experiments were carried out under effectively isothermal conditions.

2. Experimental

2.1. Catalyst samples

All experiments were performed on a commercial NOx trap catalyst supplied by Umicore Autocat USA Inc. (Auburn Hills, MI). The samples were received as cylindrical flow-through monolith bricks (11.8 cm diameter, 15.2 cm long) containing square channels at a density of 100 cells/cm^2. The washcoat, which was specifically formulated for application with gasoline direct injection (GDI) engines, contained γ-Al$_2$O$_3$, BaO and ZrO$_2$-Ce$_2$O$_3$, along with 3.99 kg/m^3 of the noble metals Pt, Pd and Rh with relative masses 82:26:6, respectively. This particular NOx catalyst has been selected by the LNT Focus Group of the DOE Crosscut Lean Exhaust Emissions Reduction Simulations (CLEERS) activity as a reference material for future collaboration (see http://www.cleers.org). Our experience with this GDI catalyst indicates that it exhibits the same basic trends in NOx reduction behavior that are seen with other LNT catalysts, both model and commercial. In fact, the Umicore catalyst is routinely used in studies of LNT behavior by diesel engine manufacturers [14,21]. Prior to experimentation, the catalyst brick was degreened in a furnace at 700 °C for 16 h under a flow of 10% water in air.

2.2. Flow reactor experiments

The apparatus, procedures, and results for the flow reactor experiments are described in detail elsewhere [12]. However, since the results from those experiments were used in mechanism development and are shown below as a basis for comparison with the simulation runs, we summarize the procedures here. A small cylindrical core sample (1.3 cm long, 2.2 cm diameter) was cut from the Umicore GDI catalyst brick and loaded into the flow reactor. The total flow rate was fixed to give a space velocity of 100,000 h^{-1} based on total monolith volume and gas flows at standard temperature and pressure. As mentioned in the Introduction, the experiments included simultaneous feed of NOx and reductant to the catalyst to decouple the reduction reactions occurring on the precious metal sites from the NOx release process. The catalyst was held under nearly isothermal conditions during slow temperature ramps. Subsequent steady-state experiments, in which the temperature was held fixed at specific levels for much longer intervals, were performed at selected conditions and confirmed that the ramped temperature conversions were close to those at true steady state [22].

Table 1
Gas feeds for steady-flow temperature-ramp experiments used in parameter determination

Species 1	Concentration	Species 2	Concentration	Molar ratio
NOx/reductant				
NO	500 ppm	H_2	500 ppm	1:1
NO	500 ppm	H_2	1250 ppm	1:2.5
NO	500 ppm	H_2	5000 ppm	1:10
NO	500 ppm	CO	500 ppm	1:1
NO	500 ppm	CO	1250 ppm	1:2.5
NO	500 ppm	CO	5000 ppm	1:10
NO_2	500 ppm	H_2	1000 ppm	1:2
NO_2	500 ppm	H_2	1750 ppm	1:3.5
NO_2	500 ppm	H_2	5000 ppm	1:10
NO_2	500 ppm	CO	1000 ppm	1:2
NO_2	500 ppm	CO	1750 ppm	1:3.5
NO_2	500 ppm	CO	5000 ppm	1:10
Secondary reactions of byproducts				
NH_3	200 ppm	O_2	200 ppm	1:1
NH_3	200 ppm	O_2	400 ppm	1:2
NH_3	200 ppm	O_2	10%	1:500
NH_3	200 ppm	NO	200 ppm	1:1
NH_3	200 ppm	–	–	–
N_2O	200 ppm	H_2	1000 ppm	1:5
N_2O	200 ppm	CO	1000 ppm	1:5
Water–gas shift				
H_2	1000 ppm	–	–	–
CO	1000 ppm	–	–	–

Note: All experiments also included 5% H_2O, 5% CO_2, and a balance of N_2.

All of the flow reactor experiments were performed with N_2 as the balance gas. Prior to each experiment, the catalyst was reduced for 30 min at 500 °C under 0.1% H_2, 5% H_2O, and 5% CO_2. It was then cooled to the desired start temperature (between 50 and 100 °C) under 5% H_2O and 5% CO_2. After the catalyst temperature stabilized, the reactant flows were initiated and the catalyst temperature was ramped to 500 °C at a rate of 5 °C/min. A total of 21 steady-flow temperature-ramp experiments were performed; the feed gas compositions for all of the experiments are shown in Table 1. All runs included 5% CO_2 and 5% H_2O. In addition to experiments with NOx and reductant (H_2 or CO), several runs were performed to identify possible secondary reactions that could lead to destruction of NH_3 and N_2O within the catalyst.

Gas temperatures were measured with 0.5 mm diameter chromel/alumel thermocouples at locations 1 cm upstream of the catalyst, inside a monolith channel at the midpoint of the core sample, and 1 cm downstream of the catalyst. Outlet concentrations of NO and total NOx were measured with chemiluminescent detectors (California Analytical Instruments Model 400-HCLD). An ammonia scrubber (Perma Pure model AS-200-08-SS) was installed upstream of the NOx analyzers. Other catalyst outlet gas concentrations (NH_3, N_2O, CO, H_2O, and CO_2) were measured with an FTIR spectrometer (Midac M2000 equipped with a Gemini Specialty Optics, 375 cm³ volume, 3 m path length gas absorption cell).

Production of N_2 was calculated assuming an instantaneous N atom balance. We recognize that storage or release of NOx during the experiment could introduce inaccuracies into the N balance, so steps were taken to minimize the probability of NOx storage. As mentioned above, the catalyst was pre-reduced to minimize the oxygen stored on the ceria sites of the catalyst, as this could otherwise promote NOx storage. Also, as indicated in Table 1, all of the NOx/reductant experiments were run under stoichiometric or net reducing conditions. Evidence of NOx storage is apparent in a few of the experiments, but we do not believe that it had a major impact on the overall selectivity results even in cases where it was observed.

2.3. DRIFTS experiments

The diffuse reflectance infrared Fourier transform spectroscopy (DRIFTS) apparatus is described elsewhere [23,24]. Briefly, it consists of a Midac M2500 spectrometer coupled with a Harrick barrel ellipse diffuse reflectance/emission sampling terminal and an integrated heated stainless steel reaction cell. The reaction cell is connected to a gas delivery manifold that incorporates a switching valve to enable exposure to varying gas compositions. The reaction cell sample holder can be heated to over 500 °C. This setup allows for observations of catalyst surface adsorbates and reaction intermediates under controlled temperatures and gas environments.

A small wafer ($\sim$5 mm $\times$ 10 mm) of wash coated monolith wall was removed from the degreened Umicore NOx trap brick and placed onto a brushed titanium substrate. The wafer and substrate were loaded into the sample holder of the DRIFTS reaction cell, and a thermocouple (0.5 mm diameter, Omega KMQIN-020G-12) was placed in contact with the catalyst wafer to measure the temperature of the surface. All DRIFTS experiments were performed with Ar as the balance gas. The sample was initially exposed to alternating streams of 300 ppm NO/10% O_2 and 0.1% H_2 (10 min each) at 500 °C to remove surface carbonates and yield the cleanest achievable background spectrum. Prior to each experiment, the catalyst was reduced in 0.1% H_2 at 500 °C for 30 min and then cooled to the desired experiment temperature under the same atmosphere.

Once the catalyst temperature stabilized, a single beam background spectrum (consisting of 100 averaged scans) was collected prior to exposure to any other gases. All spectra were collected at a resolution of 2 cm^{-1}. The backgrounds were subsequently used in converting the sample spectra to absorbance units through the following equation:

$$\text{absorbance} = -\log_{10}\left(\frac{\text{sample reflectance}}{\text{background reflectance}}\right) \quad (1)$$

In general, Kubelka–Munk (KM) units are preferred over absorbance when quantifying DRIFTS spectra. However, KM units do not differentiate between increasing and decreasing spectral features—they both appear as positive peaks in the KM spectrum. We have found that it can be quite difficult to remove all of the adsorbed carbonate species from Ba-based LNT catalysts during pretreatment steps. The residual carbonates are displaced by nitrates during NOx exposure, resulting in a decrease in spectral intensity. We use absorbance units to reveal these changes as negative peaks and differentiate them

from increased adsorbates of other species. Additionally, Meunier et al. have recently demonstrated that absorbance units are preferred to KM when baseline shifts are a concern [25]. We have found that baseline adjustments are often required for quantitative comparisons between spectra from different experiments. For these reasons, all the DRIFTS results discussed below are analyzed as absorbances.

A large set of DRIFTS experiments was performed to facilitate peak identification and identify surface species relevant to the reduction process. For conciseness, only results directly relevant to development of the reduction mechanism are reported here. Several DRIFTS experiments focused on possible reactions between NH_3 and species stored on an oxidized catalyst surface. For one set of experiments, the catalyst was exposed to 300 ppm NO and 10% O_2 for 5 min after the pretreatment described above. The reaction cell was then purged with Ar for 5 min. When the purge was complete, the catalyst was exposed to 500 ppm NH_3. DRIFTS spectra were collected every 15 s for 10 min, with each spectrum consisting of 20 scans. These nitration/reduction experiments were conducted at 200, 300, 400, and 500 °C. A second set of experiments was performed with an identical procedure except that only O_2 was fed during the initial 5 min oxidation step.

NOx storage/reduction cycles were also performed in the DRIFTS apparatus. After the usual pretreatment, the catalyst was alternately exposed to lean (6.5 min of 300 ppm NO, 10% O_2, 5% H_2O, and 5% CO_2) and rich (1 min of 0.9% H_2 or CO, 5% H_2O, and 5% CO_2) gas streams. Once the catalyst had achieved a pseudo-steady state, DRIFTS spectra were collected every 6 s (10 scans per spectrum) for three complete cycles. The background spectrum used in converting the cycle experiment sample spectra to absorbance units was taken under a flow of 5% H_2O at the same temperature as the experiment.

3. Mechanism development

In developing our elementary kinetic mechanism, we elected to focus initially on reproducing the pseudo-steady product selectivities that were determined in the bench reactor temperature-ramp experiments. The approach involved an iterative regression process whose goal was to match the available experimental data as well as possible with a reasonable number of reactions. The first step was to assemble a set of candidate reactions, together with estimates for the corresponding rate parameters (pre-exponential factors and activation energies). The catalysis literature contains discussions of many elementary reactions relevant to the present work, so these were used as a starting point in the mechanism development. However, literature values of the rate parameters are much less widely available, and the values that have been reported may not be applicable here due to differences in catalyst formulation and experimental conditions. Therefore, while we used literature values as initial guesses in the iteration process where possible, we did not use them to impose constraints on the computations. Furthermore, since it is quite possible that some of the reactions occurring in LNTs have not been discussed in the literature at all, we augmented the initial

list with candidate reactions whose presence seemed likely to improve the ability of the mechanism to describe certain aspects of the data. Not all of these reactions were added at the same time; new candidates were introduced occasionally as the need for them became apparent, while other reactions were discarded when the computations showed them to be of little significance.

Once a tentative reaction mechanism was constructed, the next step was to use it in conjunction with an appropriate reactor code to simulate the flow in a single channel of an LNT monolith. For this work we elected to use the steady-state PLUG code in the Chemkin collection [26], based upon the assumptions that (a) axial transport is strongly dominated by convection, (b) radial transport resistance is negligible, and (c) the flow is pseudo-steady due to the slowness of the temperature ramps. The first of these assumptions is justified by the large Peclet number; the second has been shown to be reasonable by carrying out simulations with the two-dimensional Chemkin CRESLAF code at the highest experimental temperature; the third has been confirmed by comparing the pseudo-steady-state results with a few simulations using a fully transient plug flow code. Thus, the gas-phase species balance used in the actual data fitting calculations was

$$\frac{D}{4} \rho u \frac{dY_i}{dx} = s_i M_i - Y_i \sum_j s_j M_j \qquad (2)$$

where D is the channel diameter, ρ the gas-phase mass density, u the axial velocity, x the axial position, Y_i the mass fraction of species i, M_i its molecular weight, and S_i is its molar production rate by surface reactions; the sum is over all gas-phase species. The species balances were solved in conjunction with the continuity equation:

$$\frac{D}{4} \frac{d}{dx}(\rho u) = \sum_j s_j M_j \qquad (3)$$

Under the assumption that there is no surface transport, the steady-state balance equation for surface species i is simply

$$s_i = 0 \qquad (4)$$

The use of the simple PLUG code in the mechanism optimization process was considered to be a practical necessity, given the extremely large number of individual runs that were involved. The resulting increase in throughput easily justified the acceptance of whatever modest errors might have been incurred.

Each simulation using the PLUG code produces a predicted set of outlet concentrations for the gas-phase species in the flow. These correspond directly to the quantities measured experimentally, so they can be used to determine a quantitative measure of the adequacy of the reaction mechanism. In this work we chose to compute a single overall figure of merit covering all of the experimental cases, all of the monitored gas-phase species, and essentially the entire temperature range. Specifically, the code was run for each inlet mixture at discrete temperatures ranging from 100 to 500 °C at intervals of 25 °C, and an overall root-mean-square deviation was computed from

all of the (appropriately scaled) deviations of the NO, NO_2, N_2O, NH_3, and CO concentrations from their respective experimental values. Since the experimental N_2 concentrations are actually inferred from a nitrogen atom balance, they cannot be regarded as independent data and were therefore not used. The overall error then served as the objective function for the parameter optimization process.

The optimization was carried out with the Sandia APPSPACK code [27], which uses an asynchronous parallel pattern search to minimize the objective function over the space of adjustable parameters. As suggested by the name, this code is designed to be run on a massively parallel machine, with each processor independently evaluating the objective function for a specified set of parameters. For a mechanism development problem, the parameter set normally consists, in principle, of the pre-exponential factors and activation energies of the candidate elementary reactions (in both forward and reverse directions), mass-action kinetics being assumed. However, in the current problem there are several complicating factors that require special consideration. Fortunately, these complexities are manifested in the form of constraints that the newest versions of APPSPACK are ideally suited to handle.

A common issue, not specific to the problem at hand, is that adjustable pre-exponential factors and activation energies tend to be tightly coupled, in the sense that the latter generally cannot be perturbed independently of the former without causing inordinately large changes in the rate constant. Stated differently, one would like to vary the magnitude of the rate constant and its temperature dependence independently, but the activation energy affects both. The solution adopted here is the so-called centering approach, in which the pre-exponential factor is replaced as an adjustable parameter by the value of the rate constant at the mid-point temperature, 300 °C. This allows the search procedure to converge much more quickly.

A complicating factor with a physical, rather than mathematical, origin is that not all of the kinetic parameters can be freely adjusted if the resulting mechanism is to be thermodynamically consistent. This arises in part from the fact that alternate pathways between the same two states must be energetically equivalent and also from the fact that the thermodynamic properties of the gas-phase species are well known. Clearly, it is crucial to know how many parameters can be specified independently and how the remainder must be constrained. The answer to this is governed by the number of adsorbed surface species involved. In addition to the obvious set of gas-phase species (O_2, NO, NO_2, CO, H_2, CO_2, N_2, H_2O, N_2O, and NH_3), all of the candidate mechanisms considered here involve 13 surface species: $()^*$, O^*, NO^*, NO_2^*, CO^*, H^*, N^*, OH^*, H_2O^*, NH^*, NH_2^*, NCO^*, and NH_3^*. The first of these is simply an empty site and, being irreducible, can be treated thermodynamically as a chemical element. Because the thermodynamic properties of the remaining 12 species are not known, any set of 12 independent surface reactions involving all of them can be designated as a core (basis) set whose equilibrium constants can be assigned arbitrarily. Thus, the kinetic parameters

(forward and reverse) for the core reactions are unconstrained, at least thermodynamically. However, each of the remaining reactions can be written as a linear combination of core surface reactions and (generally) members of a corresponding core set of fictitious gas reactions. There are 6 of the latter, given the 10 gas-phase species and 4 chemical elements, and the equilibrium constants of these reactions are well known. Therefore, the *equilibrium* constant for each of the non-core surface reactions is constrained by thermodynamics; while the kinetic parameters in one direction can still be specified arbitrarily, those in the other direction are then fixed. Besides assuring consistency, these thermodynamic constraints significantly reduce the size of the parameter space in the optimization problem, even while increasing the complexity of programming.

An additional set of constraints arises from the physical requirement that all activation energies be non-negative. This requirement is actually implemented in two distinct ways. For each activation energy that is adjusted freely, a simple bound is placed on the specified parameter space that is searched for the desired optimum. For each activation energy whose value is determined by a thermodynamic constraint, the additional non-negativity constraint takes the form of a linear inequality involving the activation energies that *are* adjustable. Fortunately, APPSPACK is equipped to handle just this kind of situation, which basically places a new set of oblique bounds on the already constrained parameter space.

After APPSPACK has converged on an apparent minimum of the objective function, there are still some remaining questions. As usual, it is possible that the code has found merely a local minimum or that it has terminated prematurely without finding a minimum at all. While it is generally impossible to resolve this issue completely, a reasonable approach is to perturb the optimized parameters to a modest degree and then to repeat the search procedure. The results obtained in this way usually improve for a few cycles before settling down in the neighborhood of a more robust minimum. Of course, the existence of numerous shallow local minima is not unexpected in a many-dimensional parameter space.

A final question is whether all of the candidate reactions in the optimized mechanism really contribute significantly to the simulation results; obviously, superfluous reactions should be discarded in the interest of computational efficiency, even if they appear to be physically reasonable. Our approach to this question involves two steps. First, reactions (non-core only) are dropped from the mechanism one at a time and the entire suite of simulations is rerun each time, without altering the remaining parameters, in order to gauge the effects on the fit. For each reaction that appears to be of minor importance, based on the value of the objective function, the second step is to redo the entire optimization procedure with the reaction absent. In theory this can only lead to a degradation of the fit, but in many cases the change is nearly imperceptible, whereupon the reaction in question can be permanently discarded. Many iterations of this procedure have led to a final mechanism that is presumably free of inconsequential reactions.

4. Final mechanism

The reaction mechanism ultimately resulting from the above development process is shown in Table 2. Associated with each reaction are sets of Arrhenius rate parameters for both the forward and reverse directions, defined by the conventional

formula:

$$k = AT^n \exp\left(\frac{-E}{RT}\right) \tag{5}$$

where k is the unidirectional rate constant, T the absolute temperature, and R is the universal gas constant. Each activa-

Table 2
Reactions in the surface mechanism and the corresponding kinetic parameters

No.	Reaction	A (cgs units)	n	E (kJ/mol)	Core reaction?	Irreversible?
Simple adsorption/desorption						
(S1)	$NO + ()^* = NO^*$	1.252E+17	0.0	50.56	✔	
		1.302E+17	0.0	104.13		
(S2)	$NO_2 + ()^* = NO_2{}^*$	8.934E+15	0.0	16.46	✔	
		2.625E+17	0.0	79.82		
(S3)	$CO + ()^* = CO^*$	7.786E+22	0.0	99.27	✔	
		4.015E+13	0.0	78.54		
(S4)	$H_2O^* = H_2O + ()^*$	1.222E+17	0.0	78.43	✔	
		4.471E+19	0.0	59.36		
(S5)	$NH_3 + ()^* = NH_3{}^*$	1.003E+31	0.0	173.49	✔	
		2.072E+27	0.0	185.08		
Dissociative adsorption/desorption						
(S6)	$O_2 + 2()^* = 2O^*$	1.775E+24	0.0	21.92	✔	
		1.919E+36	0.0	230.41		
(S7)	$H_2 + 2()^* = 2H^*$	2.193E+26	0.0	59.06	✔	
		9.936E+25	0.0	88.74		
(S8)	$CO^* + O^* = CO_2 + 2()^*$	4.045E+15	0.0	2.43		✔
		4.681E+23	−0.8624	204.11		
(S9)	$2N^* = N_2 + 2()^*$	1.395E+19	0.0	86.96		✔
		2.052E+17	0.0490	165.18		
(S10)	$NO^* + N^* = N_2O + 2()^*$	1.570E+12	0.0	25.14		✔
		1.302E+15	−0.5508	19.54		
(S11)	$2N^* + O^* = N_2O + 3()^*$	9.548E+35	0.0	157.90		
		2.529E+31	−0.5508	50.48		
Surface decomposition/recombination						
(S12)	$NO^* + ()^* = N^* + O^*$	6.931E+22	0.0	96.63	✔	
		2.168E+30	0.0	198.45		
(S13)	$NO^* + O^* = NO_2{}^* + ()^*$	2.402E+31	0.6102	203.72		
		1.512E+30	0.0	167.99		
(S14)	$H^* + OH^* = H_2O^* + ()^*$	3.384E+25	0.0	15.11		
		4.922E+28	0.627	155.30		
(S15)	$H^* + O^* = OH^* + ()^*$	1.468E+43	0.0	162.40	✔	
		7.275E+29	0.0	146.47		
(S16)	$NH_3{}^* + ()^* = NH_2{}^* + H^*$	9.473E+20	0.9115	115.45		
		2.743E+31	0.0	141.82		
(S17)	$NH^* + H^* = NH_2{}^* + ()^*$	4.237E+15	0.0	16.30	✔	
		7.918E+24	0.0	100.28		
(S18)	$N^* + H^* = NH^* + ()^*$	1.241E+26	0.0	89.74	✔	
		1.160E+21	0.0	80.15		

Table 2 (*Continued*)

No.	Reaction	A (cgs units)	n	E (kJ/mol)	Core reaction?	Irreversible?
Atom transfer						
(S19)	$NH_3^* + O^* = NH_2^* + OH^*$	7.709E+22	0.0	52.33		✔
		1.106E+20	−0.9115	62.72		
(S20)	$O^* + NH^* = OH^* + N^*$	1.275E+13	0.0	29.86		✔
		6.762E+04	0.0	23.52		
(S21)	$NO^* + H^* = N^* + OH^*$	1.329E+16	0.0	33.29		✔
		2.062E+10	0.0	119.18		
(S22)	$NO_2^* + H^* = NO^* + OH^*$	2.245E+15	0.0	32.64		✔
		1.768E+03	0.6102	52.44		
(S23)	$N_2O + H^* = N_2 + OH^*$	8.330E+18	0.0	78.15		✔
		2.292E+08	0.5998	247.86		
Atom transfer with adsorption/desorption						
(S24)	$2NO^* = N_2O + O^* + (\ )^*$	6.533E+25	0.0	108.68		✔
		1.694E+36	−0.5508	204.90		
(S25)	$NO_2^* + CO^* = NO^* + CO_2 + (\ )^*$	6.553E+20	0.0	61.40		✔
		1.204E+30	−0.2522	298.82		
Water–gas shift reaction						
(S26)	$H_2O^* + CO^* = 2H^* + CO_2$	4.038E+19	0.0	84.70		
		6.480E+37	−1.489	162.13		
Isocyanate formation and hydrolysis						
(S27)	$N^* + CO = NCO^*$	9.243E+20	0.0	106.91	✔	
		7.979E+15	0.0	125.66		
(S28)	$NCO^* + H_2O^* = NH_2^* + CO_2 + (\ )^*$	8.455E+23	0.0	103.85		
		1.416E+42	−1.4894	216.19		

tion energy E was taken to be a constant, i.e., independent of the local surface composition. The temperature exponent n was *not* used as a fitting parameter; thus, it is zero in both directions for each of the 12 core reactions indicated. It was also defined to be zero for each of the non-core reactions in one direction, but the imposition of the thermodynamic constraint can in general lead to a nonzero value in the other direction, as will become clear shortly. To reiterate, all four of the Arrhenius parameters A and E associated with a given core reaction were adjustable (subject to the centering technique discussed above), but only two of those associated with a non-core reaction (one A and one E) were likewise free to be varied. Thus, for the 28 reactions in the mechanism, there were 80 adjustable parameters, as opposed to 112 in the absence of thermodynamic constraints. Whether the constraints are applied to the forward or reverse parameters is arbitrary and of no consequence. The number of adjustable parameters was certainly large, but it was still far smaller than the 1785 data points used in the fitting process.

In accordance with the accepted Chemkin convention, the pre-exponential factors in Table 2 are expressed in concentration (as opposed to, for example, pressure or mole fraction) units. Together with the assumption of mass-action kinetics, this determines the form of each of the rate expressions. As an example, for reaction (S1) the net forward rate is

$$r_{S1} = k_{S1}c_{NO}c_{(\ )*} - k_{-S1}c_{NO*} \tag{6}$$

The concentration c for a gas-phase species is the product of P/RT and the mole fraction, while c for a surface species is the product of the overall surface site density (for the precious metal phase) and the site fraction. It is important to note that the pre-exponential factors in Table 2 refer to a site density of 2.85×10^{-9} mol/cm^2. While this is a nominal value for a platinum catalyst [28], the value chosen is actually completely arbitrary in this case; for a system at steady state, it is easily shown that the site density can be scaled out of the problem and is therefore indeterminate via data fitting. Stated differently, the site density could be lumped with the rate constants rather than used explicitly. Still, it must be recognized that the pre-exponentials in Table 2 refer *specifically* to the stated value, so the site density must not be changed without making appropriate adjustments in the other parameters. Lastly, it is clear from the list of surface species that no attempt is being made here to distinguish between the different roles of the three precious metals (platinum, palladium, and rhodium) in the catalyst; only their combined influence is simulated. While this undoubtedly obscures some details, it was deemed necessary for practical

reasons and certainly provides a useful first approximation for device simulation applications. It can also serve as a starting point for efforts to resolve the roles of the individual metals, such work being central to the development of improved catalyst formulations.

The last column in Table 2 shows which reactions were found to be essentially irreversible (in the direction written). While complete reversibility must be assumed during the data fitting process in order to assure thermodynamic consistency, sensitivity analyses showed that many of the reverse reactions could be deleted with no noticeable effect. This could possibly be exploited in future use of the mechanism as a means of reducing numerical stiffness.

Table 3 shows the fictitious gas-phase reactions that are used in formulating thermodynamic constraints for the non-core surface reactions. With the understandable exception of (G3), these are just the formation reactions for the non-elemental gas-phase species appearing in the surface mechanism. Also given are data for the equilibrium constants in the form:

$$K = ZT^n \exp\left(\frac{-Q}{RT}\right) \tag{7}$$

The stated values have been computed from the polynomial coefficients in the Chemkin thermodynamic database [26] by fitting calculated free energies of reaction over the same temperature range used in the steady-flow experiments. The equilibrium constants have been converted from pressure to concentration units in order to make them directly usable with the thermodynamic constraints.

Table 4 shows how each of the non-core surface reactions is expressed (uniquely) in terms of the core reactions, both gas-phase and surface. For each of the equations there is a corresponding relation between the equilibrium constants; for example

$$K_{S8} = K_{S6}^{-1/2} K_{S3}^{-1} K_{G3} \tag{8}$$

The K values for the gas-phase reactions have just been discussed, while those for the surface reactions are expressed as ratios of rate constants written in terms of Arrhenius parameters. Matching the corresponding factors on the two sides of the equation provides the desired thermodynamic constraints;

Table 3
Gas-phase reactions used in formulating the thermodynamic constraints

No.	Reaction	Z (cgs units)	n	Q (kJ/mol)
(G1)	$\frac{1}{2}N_2 + \frac{1}{2}O_2 = NO$	3.793E+00	0.0245	90.26
(G2)	$\frac{1}{2}N_2 + O_2 = NO_2$	1.638E−03	0.6347	31.54
(G3)	$CO + \frac{1}{2}O_2 = CO_2$	1.612E−05	0.8624	−285.20
(G4)	$H_2 + \frac{1}{2}O_2 = H_2O$	8.046E+01	−0.627	−239.11
(G5)	$N_2 + \frac{1}{2}O_2 = N_2O$	5.338E−04	0.5998	81.40
(G6)	$\frac{1}{2}N_2 + \frac{3}{2}H_2 = NH_3$	1.362E+02	−0.887	−41.89

Table 4
Relations between the non-core and core reactions

(S8) = −1/2(S6) − (S3) + (G3)
(S9) = (S6) − 2(S1) − 2(S12) − 2(G1)
(S10) = 1/2(S6) − 2(S1) − (S12) − 2(G1) + (G5)
(S11) = 1/2(S6) − 2(S1) − 2(S12) − 2(G1) + (G5)
(S13) = −1/2(S6) − (S1) + (S2) − (G1) + (G2)
(S14) = −1/2(S6) − (S7) − (S15) − (S4) + (G4)
(S16) = −1/2(S6) + (S1) + 3/2(S7)
+ (S12) + (S18) + (S17) − (S5) + (G1) − (G6)
(S19) = −1/2(S6) + (S1) + 3/2(S7) +
(S12) + (S15) + (S18) + (S17) − (S5) + (G1) − (G6)
(S20) = (S15) − (S18)
(S21) = (S12) + (S15)
(S22) = 1/2(S6) + (S1) − (S2) + (S15) + (G1) − (G2)
(S23) = 1/2(S6) + (S15) − (G5)
(S24) = 1/2(S6) − 2(S1) − 2(G1) + (G5)
(S25) = (S1) − (S2) − (S3) + (G1) − (G2) + (G3)
(S26) = −(S3) + (S7) + (S4) + (G3) − (G4)
(S28) = (S7) + (S4) + (S18) + (S17) − (S27) + (G3) − (G4)

for example, Eq. (8) implies that

$$A_{-S8} = A_{S8}\left(\frac{A_{S6}}{A_{-S6}}\right)^{1/2} \frac{A_{S3}}{A_{-S3}} \cdot \frac{1}{Z_{G3}} \tag{9}$$

$$n_{-S8} = -n_{G3} \tag{10}$$

and

$$E_{-S8} = E_{S8} + \frac{1}{2}(E_{S6} - E_{-S6}) + E_{S3} - E_{-S3} - Q_{G3} \tag{11}$$

where a negative subscript refers to the reverse reaction. As noted above, this explains why some of the rate constants have nonzero temperature exponents. Use of all 16 relations in Table 4 guarantees thermodynamic consistency both internally and with known gas-phase data.

Turning to a discussion of the surface reactions themselves, we can state that most of them are familiar and/or expected but that a few are surprising. Reactions (S6), (S7), (S15), (S14), and (S4) constitute a mechanism for the catalytic combustion of hydrogen and have been considered by, for example, Fridell et al. [29]. Reactions (S1), (S2), and (S13) allow for the interconversion of NO and NO_2 and have been discussed by Olsson et al. [30]. Reactions (S18), (S17), (S16), and (S5) provide a straightforward pathway for ammonia synthesis and decomposition; Hecker and Bell [31] use the first two of these as well as a combined version of the second two. N_2O production via reactions (S10) and (S24) has been proposed by Burch et al. [32]. Reactions (S21) and (S22) are obvious steps in the reduction of adsorbed NOx by hydrogen; the former appears in the mechanism of Hecker and Bell [31]. Reaction (S25) is clearly the analog of (S22) with CO rather than H serving as the reductant. The two most basic steps involving CO, namely (S3) and (S8), are contained in the mechanism of Hoebink et al. [28], as are the equally obvious reactions (S12) and (S9). Reactions (S19) and (S20) are logical steps in the oxidation of ammonia; a reaction involving NH_2^* could be included as well but is found to be noncontributing. Reaction

(S23) provides for direct reduction of N_2O by hydrogen, although this process could also proceed stepwise via reactions (S10), (S21), and (S9).

Reaction (S11) is clearly unusual in being third order with respect to surface species. This reaction has been introduced specifically to account for a puzzling experimental fact, namely that oxidation of NH_3 produces very significant amounts of N_2O, while reduction of N_2O (by either H_2 or CO) produces no measurable NH_3. Generally, an attempt to reconcile the mechanism with one of these observations tends to destroy its ability to match the other. Reaction (S11) helps to alleviate this problem by allowing N_2O to be formed directly from surface fragments that would otherwise form the very stable N_2. Regardless of any mechanistic questions about this reaction, it still satisfies its own thermodynamic constraint and therefore cannot be questioned on the basis of overall energetics.

One of the more interesting challenges in explaining the experimental data is determining the actual route for NH_3 production during the reduction of NOx by excess CO. The hydrogen source is obviously the H_2O in the background gas, but the operative mechanism for water splitting is less clear. A logical candidate is the well-known water–gas shift (WGS) reaction, step (S26) in our mechanism; this version may not actually be completely elementary, but it seems to work very well. However, during the NOx/CO temperature ramps, NH_3 production is well underway at temperatures below that at which the WGS reaction commences, this light-off temperature being determined independently by a ramp using CO but no NOx. Furthermore, the CO consumption during a NOx/CO ramp tends to occur over two distinct temperature ranges, with only the first being associated with NH_3 production. Thus, it appears that there is a second water-splitting mechanism to complement the WGS reaction and that this second process is in fact primarily responsible for NH_3 formation. A likely route involves the adsorbed isocyanate species NCO[*], whose existence has been confirmed by Hecker and Bell [33] and whose formation is proposed by them to be given by reaction (S27). The subsequent hydrolysis of this species probably proceeds according to reaction (S28) or something very similar; again, this step may not be completely elementary. Clearly, the combination of reactions (S27) and (S28) is equivalent to the WGS process, except that the released hydrogen atoms are already tied to nitrogen, so that the path to NH_3 is nearly complete.

Together, the 28 surface reactions are able to reproduce the pseudo-steady experimental bench reactor data from the temperature ramps (specifically, the observed product distributions) remarkably well over the entire range of temperatures and inlet gas compositions. It should be remembered, however, that the mechanism has been designed and optimized to match *this* data set and is therefore not as general as it could possibly be. As one obvious example, it does not address the use of reductants other than H_2 and CO. Also, it can be expected to perform best under reducing conditions, although it certainly does include the NO/NO_2 interconversion reactions that take place on precious metal sites during the storage phase of LNT operation.

Finally, as noted earlier, this mechanism is by no means a comprehensive list of reactions that could play a role in LNT regeneration, even under the restrictions just mentioned. There are many apparent omissions, such as the analog of reaction (S25) that describes reduction of NO[*] rather than NO_2[*]. Again, the final mechanism is thought to include all those reactions that give a noticeable improvement in the quality of the overall data fit but to exclude those that, while sensible, appear to be of minimal importance.

5. Results and discussion

5.1. Simulation results and comparison to experiments

The reaction mechanism in Table 2 is designed to provide the best overall fit to 21 separate experimental cases (temperature ramps), namely the 12 involving reduction of NO or NO_2, the 7 dealing with secondary reactions of NH_3 or N_2O, and 2 using just H_2 or CO as a reactant. All of the cases are simulated quite well, but there is sufficient space here to show and discuss only a sampling of them. From these all of the important conclusions can be drawn.

Fig. 1 shows the experimental and computed results for a feed of NO and H_2 that is stoichiometric for N_2 production. Note that the markers on the experimental curves are solely for ease of identification; the actual data are plotted at roughly 1 °C intervals. The simulation reproduces the most important observations, namely that N_2 is indeed the dominant product above about 250 °C but that a mixture of N_2, NO, N_2O, and NH_3 results at lower temperatures. It should be remembered that the experimental N_2 concentration is calculated by difference from directly measured quantities and is therefore subject to more uncertainty; in particular, any loss of N atoms due to adsorption of NO on storage sites would cause the N_2 production to be overstated. This should not be a major problem under reducing conditions but should still be kept in mind for this and subsequent cases.

Fig. 2 shows results for the case in which the H_2/NO ratio is now 2.5 times its stoichiometric value. Again, the overall agreement is quite satisfactory. As expected, the substantial excess of H_2 leads to a large amount of NH_3 production over most of the temperature range. However, this is depressed at the highest temperatures by NH_3 decomposition and by H_2 consumption via the water–gas shift reaction, both of which can be simulated separately and were, in fact, included in the data fitting.

Fig. 3 shows results for a case in which NO_2, rather than NO, is fed to the reactor with an excess of H_2. The apparent production of N_2 at low temperatures and its surge at around 250 °C are probably artifacts (possibly due to storage) that the simulation has no real chance of reproducing. Furthermore, the computed product mix at temperatures below about 250 °C is only roughly correct. The data fit for this case is, in fact, one of the two poorest of all 21; the results for a 1:10 ratio of NO_2 to H_2 are slightly worse. Still, the simulation correctly shows that
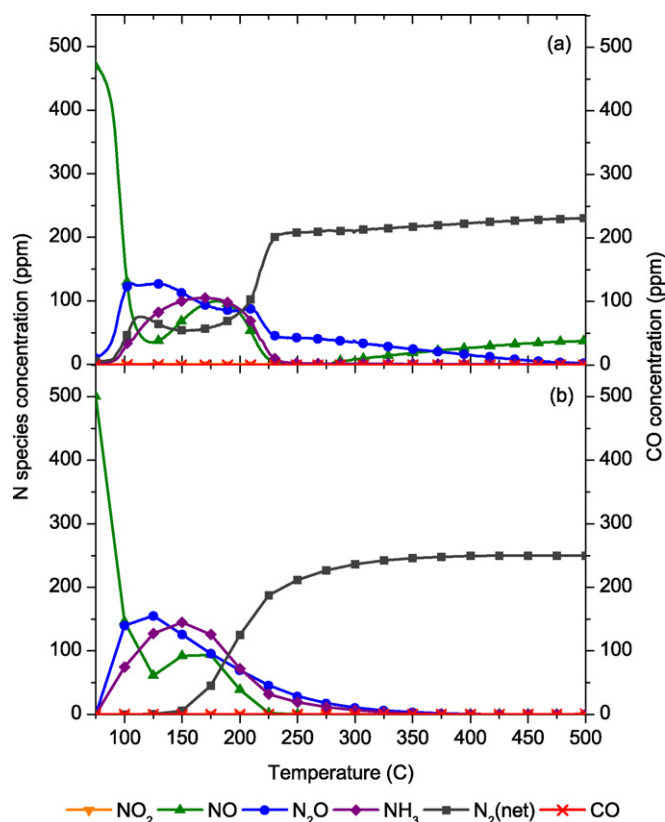
Fig. 1. Outlet gas-phase concentrations vs. temperature for an inlet mixture containing 500 ppm NO and 500 ppm H_2: (a) experimental measurements; (b) simulation results.
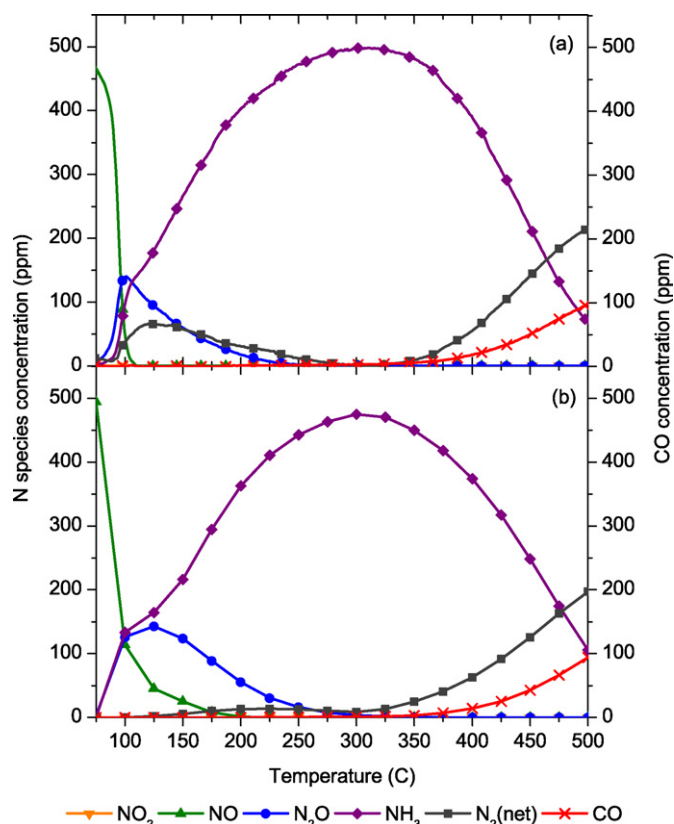

Fig. 2. Outlet gas-phase concentrations vs. temperature for an inlet mixture containing 500 ppm NO and 1250 ppm H_2: (a) experimental measurements; (b) simulation results.

NO_2 is fully reduced to NH_3 (subject again to decomposition) at all but the lowest temperatures, where some NO is produced but NO_2 is largely unreacted.

Fig. 4 shows the interesting and informative case in which NO_2 is fed with a very large excess of CO. The amount of reductant is so excessive that NH_3 remains the dominant reaction product even at the highest temperatures. Furthermore, there is little unreacted NO_2 even at low temperatures, although the simulation exaggerates the amount somewhat. However, the most notable feature in the experimental results is the striking two-step drop in the outlet CO concentration. As noted in the previous section, this is strong evidence for the existence of two distinct pathways for CO consumption, only one of which is related to NOx reduction. Ironically, the simulation results show that the mechanism incorporating these pathways almost completely smoothes out the transition between them. Nevertheless, it is easily shown that both of them are crucial to any successful fitting of the data.

Turning to the secondary data sets, Fig. 5 shows results for the reduction of N_2O by excess H_2. The experimental results are quite simple and perhaps surprisingly so: Despite the large excess of reductant, there is no measurable production of NH_3. By contrast, the mechanism predicts a small but noticeable generation rate for this species. It is actually very easy to modify the mechanism to eliminate this minor deficiency, which is traceable largely to reaction (S11). However, as mentioned in the previous section, it then becomes nearly

impossible to account for the production of N_2O during NH_3 oxidation, to be discussed next. In any case, Fig. 5 also shows very clearly the result of the high-temperature reverse water–gas shift reaction, which predictably converts CO_2 to CO using part of the unreacted H_2.

Oxidation of NH_3 in a 1:2 mixture with O_2 is shown in Fig. 6. Not surprisingly, a range of products is observed, with more heavily oxidized species appearing at higher temperatures. The model is able to reproduce all of the results quite well. The predictions remain acceptable even under strongly oxidizing conditions, as shown in Fig. 7. Here the NH_3/O_2 ratio is 1:500, as might be encountered just after lean combustion has resumed. Aside from an onset temperature for NO that is too low by about 50 °C, the simulation results are still quite accurate. This case is especially interesting in showing the whole range of species, from fully reduced to fully oxidized. Even more than Fig. 3, it suggests that the mechanism is sufficiently robust to handle the wide range of conditions that might be encountered in practice.

As noted earlier, in electing to use the Chemkin PLUG code to carry out the parameter optimization, we verified that the steady-state and plug flow assumptions were generally valid. After the optimization was complete, we performed a more comprehensive verification by simulating all of the temperature-ramp experiments with a transient one-dimensional code that accounts for radial gas-phase mass-transfer resistance. This code computes the mass-transfer coefficient from a correlation
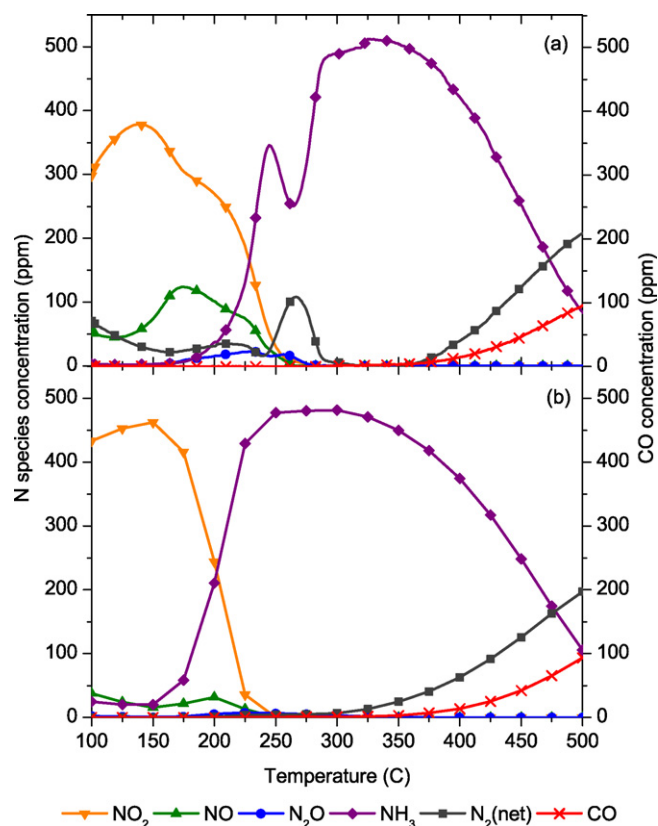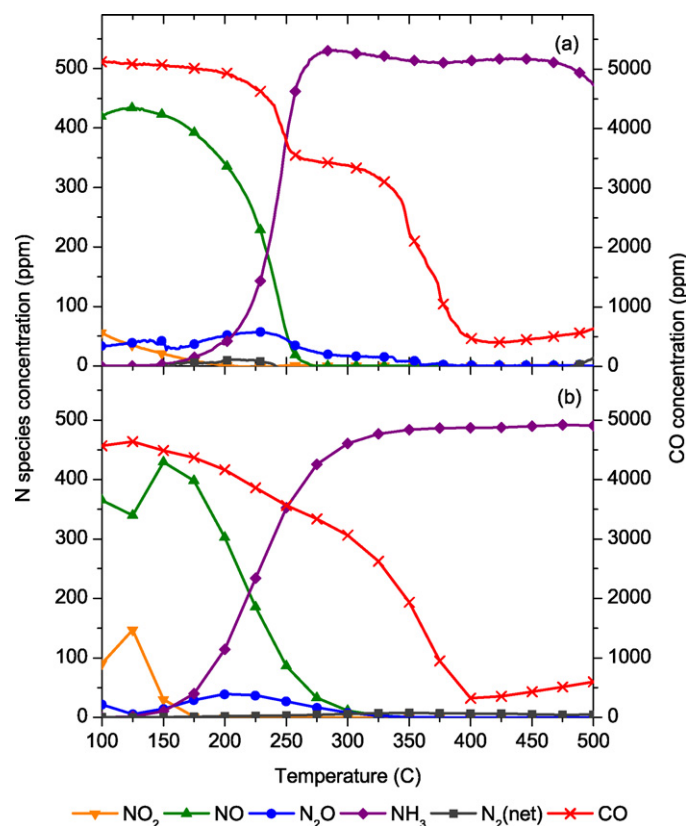
Fig. 3. Outlet gas-phase concentrations vs. temperature for an inlet mixture containing 500 ppm NO_2 and 1750 ppm H_2: (a) experimental measurements; (b) simulation results.

Fig. 4. Outlet gas-phase concentrations vs. temperature for an inlet mixture containing 500 ppm NO_2 and 5000 ppm CO: (a) experimental measurements; (b) simulation results.

for the Sherwood number of a developing laminar boundary layer [34]. These simulations confirmed that the assumptions underlying the PLUG code are well satisfied in most of the experimental cases. However, some possible exceptions were noted for the three NH_3 oxidation runs. The results in these cases suggested that mass transfer may actually be rate limiting in roughly the 200–300 °C temperature range, as can be seen by comparing Figs. 6(b) and 8(a). As confirmation of this, when the Sherwood number from the correlation is increased by a factor of 5, as in Fig. 8(b), mass transfer is sufficiently rapid that it no longer limits the rate, and the results agree well with those in Fig. 6(b).

In spite of these observations, it cannot be concluded that mass-transfer resistance is definitely a factor in the NH_3 oxidation cases, because the applicability of the Sherwood number correlation to monolith channels is uncertain. Although the flow is expected to be mostly laminar, measured mass transfer rates in these channels have often been found to deviate significantly from values calculated using laminar boundary layer correlations [35–37]. Various explanations for such deviations have been provided in the literature [35,37]. For example, the roughness and/or porosity of the washcoat may be responsible. Alternatively, it has been suggested that the flow is not laminar throughout a monolith channel. For flow rates typical of engine exhaust, the flow is often turbulent upstream of the monolith and may not immediately become laminar as it enters the channels. Turbulent fluctuations persisting for some

distance into a channel may greatly enhance the mass transfer rate. Therefore, it is possible that the mass transfer rate in our experiments was much higher than that given by the laminar boundary layer correlation.

On a separate note, we should mention that the three NH_3 oxidation experiments are also the only cases in which NOx storage on the sorbent sites is likely. Because the overall flow is either neutral or lean relative to N_2 production, the oxidation of NH_3 inevitably produces some NOx, which can then be stored. Therefore, the applicability of the current mechanism to the NH_3 oxidation cases should be reevaluated after reactions involving the NOx storage sites have been added.

Finally, it is necessary to point out a feature of the mechanism that would not be obvious from the kind of simulation results just presented. Close examination shows that at least six of the cases have multiple steady-state solutions over narrow but finite ranges of temperature (never wider than 20 °C; multiplicity over a range entirely within one of the 5 °C sampling intervals used here would go undetected). Specifically, this occurs for all of the inlet mixtures containing CO and either NO or NO_2. Intuitively, the occurrence of multiplicity in these cases could be attributed to the existence of several distinct pathways for the reduction of NOx by CO. As confirmation of this, it is found that the multiplicity disappears when the isocyanate hydrolysis reaction (S28) is deleted from the mechanism, although the predictions are then quite poor. The existence of multiple steady states is an interesting
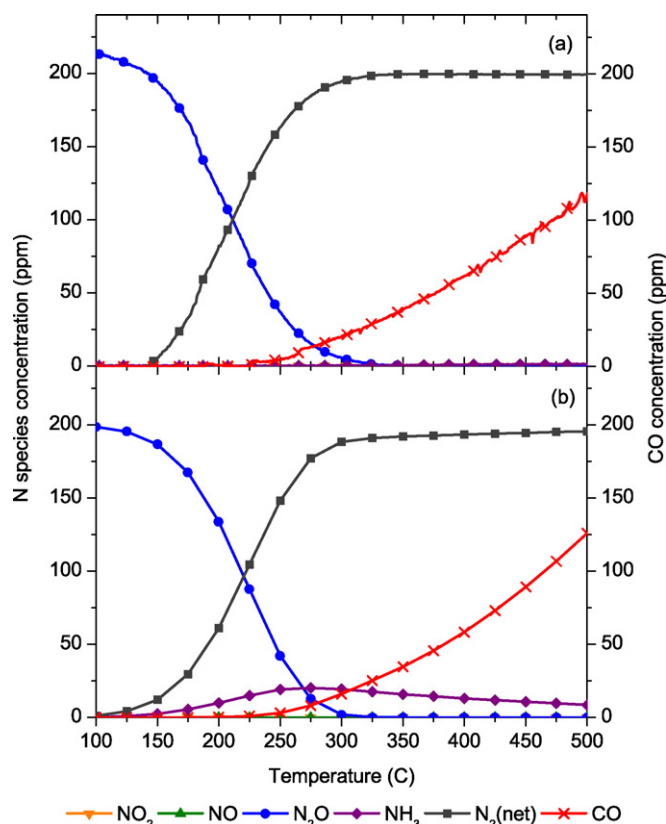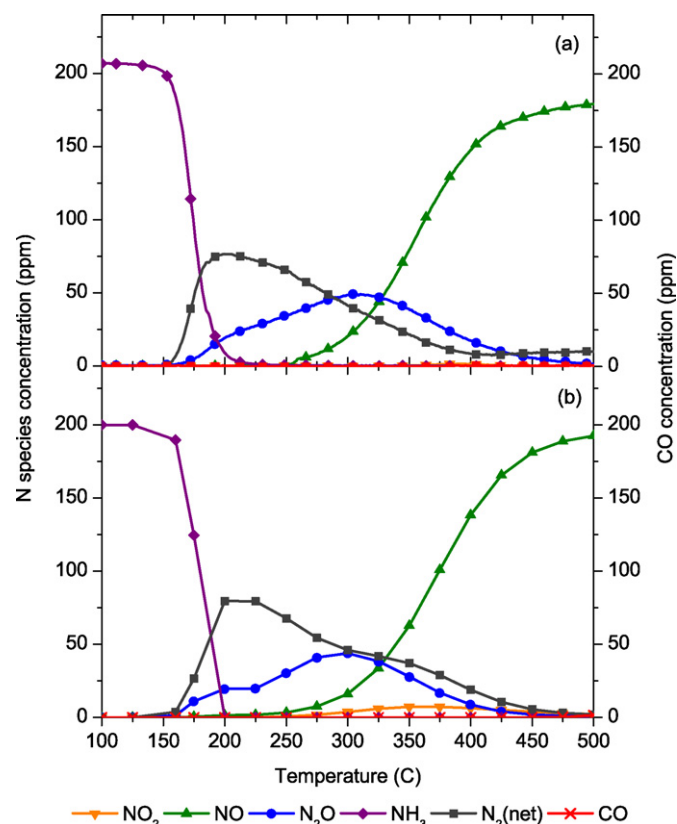
Fig. 5. Outlet gas-phase concentrations vs. temperature for an inlet mixture containing 200 ppm N_2O and 1000 ppm H_2: (a) experimental measurements; (b) simulation results.

Fig. 6. Outlet gas-phase concentrations vs. temperature for an inlet mixture containing 200 ppm NH_3 and 400 ppm O_2: (a) experimental measurements; (b) simulation results.

mathematical phenomenon and has been shown to occur in many chemical systems, so it is worth further investigation.

Fig. 9 shows a portion of the simulated temperature ramp for the case 1:2.5 NO/CO, as computed once again from the Chemkin steady-state PLUG code but at many new temperatures. Note that each of the indicated points represents a separate run of the code and that these runs have no connection with each other. The two branches are obtained by using two different guesses for the surface composition at the entrance to the reactor; such a guess is required by the PLUG code, but ordinarily it has no effect on the final results. In this case there are obviously two distinct solutions at temperatures between about 150 and 164 °C. The upper branch has an apparent discontinuity at the lower end of the multiplicity range, while the lower branch has sharp kinks both at the upper end and at about 156 °C. Of course, these actual values are not important, as they undoubtedly depend on the details of the reaction mechanism, but the existence of these features is potentially significant.

The most obvious question at this point is how these pseudo-steady-state results compare with the actual time-dependent behavior during the slow temperature ramp. As a result of transient effects, the system could be expected to follow a smooth, continuous path across the transition region, but the manner in which it might choose (or interpolate) between the two pseudo-steady-state solutions is not at all obvious. To

answer this question, we have carried out simulations using a fully transient Chemkin-based plug flow code that uses finite differences in the spatial direction and the DASAC code [38] for the time integration. Fig. 10 shows the results over the same temperature range as considered above. In contrast with Fig. 9, each of the two curves here is obtained from a single run of the transient plug flow code, so it represents the actual time-dependent behavior of the reactor. The solid curve corresponds to an increasing temperature ramp, as in the actual experiment, while for the dashed curve the temperature is ramped downward. Interestingly, the forward sweep follows the lower branch of Fig. 9 almost perfectly, despite the kinks, thus providing strong support for the initial pseudo-steady-state assumption. On the other hand, the reverse sweep drops gradually rather than abruptly from the upper to the lower steady-state branch, so technically the assumption of pseudo-steady-state behavior fails here. More interesting, however, is the undeniable hysteresis in the results, which is a standard feature of systems exhibiting steady-state multiplicity.

Because our reaction mechanism must be regarded as a proposal rather than a fully verified description of the detailed surface chemistry, it would be premature to claim that steady-state multiplicity should be observable in an actual LNT. However, if evidence of multiplicity is eventually obtained, then the mechanism presented here should be looked upon as providing a reasonable explanation.
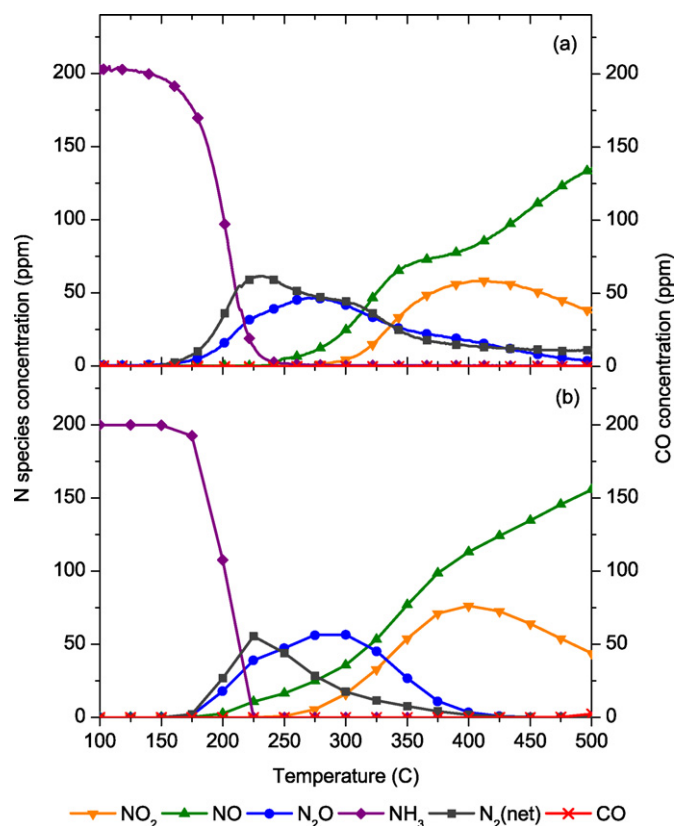
Fig. 7. Outlet gas-phase concentrations vs. temperature for an inlet mixture containing 200 ppm NH$_3$ and 10% O$_2$: (a) experimental measurements; (b) simulation results.

5.2. DRIFTS results

Figs. 6 and 7 illustrate that NH$_3$ is readily oxidized by O$_2$ over the LNT catalyst. A separate experiment performed with 500 ppm NO and 500 ppm NH$_3$ showed similar behavior, with complete consumption of the NH$_3$ fed to the catalyst over most of the temperature range studied. These results led us to postulate that NH$_3$ formed during the regeneration process reacts with stored oxygen and/or NOx in the downstream (unregenerated) portions of the catalyst, preventing NH$_3$ slip until the catalyst surface is almost completely reduced [12]. This conjecture explains why NH$_3$ slip typically coincides with reductant breakthrough, and it motivates the inclusion of steps leading to NH$_3$ oxidation in the final reduction mechanism. However, the flow reactor experiments simultaneously exposed the catalyst to gaseous NH$_3$ and oxidants, and therefore did not explicitly investigate reactions with stored O$_2$ and NOx. We conducted DRIFTS experiments to study this chemistry further.

The first set of experiments involved storing NOx on the catalyst surface (5 min of 300 ppm NO and 10% O$_2$), purging the reaction cell with Ar, and then exposing the catalyst to 500 ppm NH$_3$. Fig. 11 shows the DRIFTS spectra collected during NH$_3$ exposure at 300 °C. The spectral features between 1310 and 1475 cm^{-1} are all due to nitrates and nitrites stored on the catalyst [39]. As the NH$_3$ exposure proceeds, the nitrates and nitrites on the surface steadily decrease until the catalyst is completely regenerated after 10 min. Similar results (not shown

here) were obtained at 200 and 400 °C. These experiments confirm that NH$_3$ can react with NOx stored on the catalyst surface; in fact, it is quite a good reductant for regenerating the LNT [17].
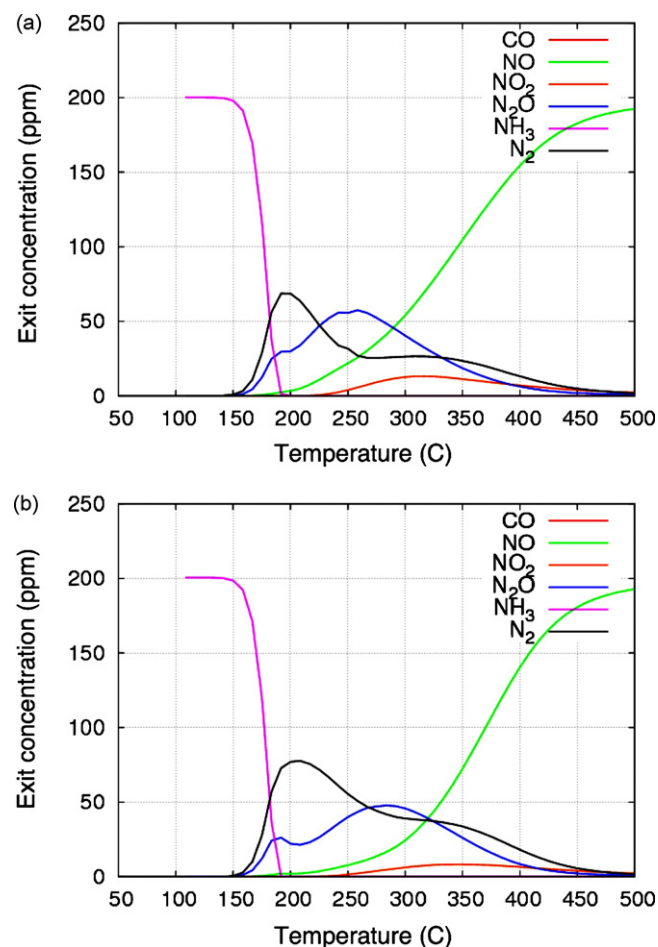
Fig. 8. Outlet gas-phase concentrations vs. temperature for an inlet mixture containing 200 ppm NH$_3$ and 400 ppm O$_2$, as computed from a one-dimensional transient flow code with boundary layer mass transfer: (a) mass transfer coefficient from standard correlations; (b) mass transfer coefficient increased by a factor of 5.
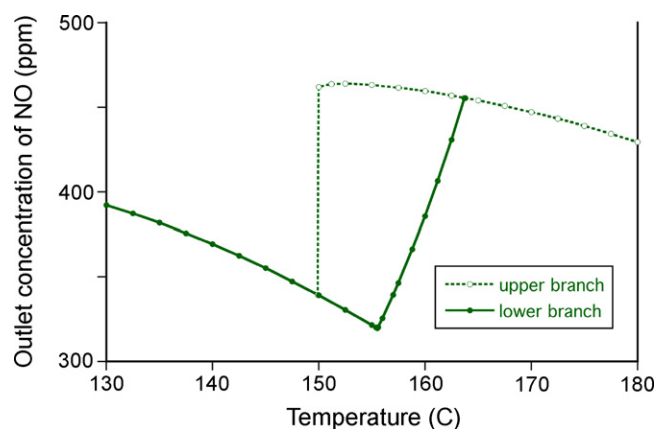

Fig. 9. Pseudo-steady simulation of temperature ramp for an inlet mixture containing 500 ppm NO and 1250 ppm CO.
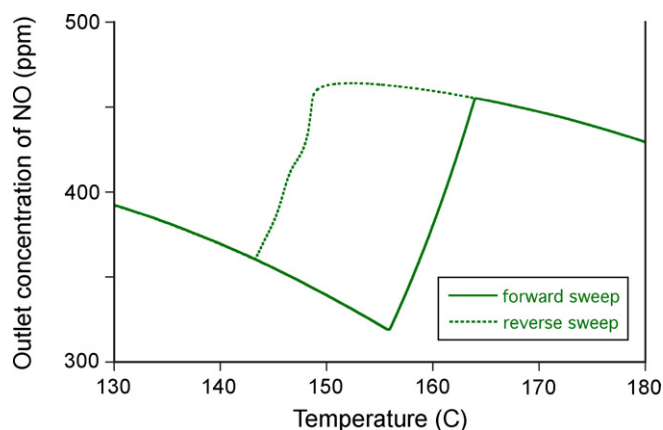
Fig. 10. Fully transient simulations of temperature ramp for an inlet mixture containing 500 ppm NO and 1250 ppm CO.

This procedure was repeated in a second set of experiments with only 10% O_2 fed during the initial storage step. The DRIFTS spectra collected during the NH_3 exposure at 200 °C are shown in Fig. 12. As the exposure proceeds, an absorbance peak grows in at around 1225 cm^{-1}, reaches its maximum amplitude at around 3 min, and then decreases to background levels after 7 min. This peak has been identified through NO exposure experiments in our laboratory and in the literature as surface nitrites [39]. Formation of nitrites indicates that the NH_3 initially reacts with the oxygen species stored on the catalyst surface. As the exposure proceeds, the NH_3 depletes

the stored oxygen species and eventually reduces the previously stored nitrites, regenerating the catalyst surface. The same processes were observed at 300 and 400 °C, although at a faster rate. Together with the previous set of experiments, these results validate our previously stated hypothesis regarding oxidation of NH_3 (formed during regeneration) by stored NOx and oxygen species in the downstream portions of the catalyst.

As discussed in the mechanism description, one of the pathways for reduction of NOx by CO involves hydrolysis of adsorbed isocyanate species (NCO*). We conducted a series of DRIFTS experiments to determine the feasibility of this feature of the mechanism. Experiments performed over a wide range of temperatures with NO and CO in the feed generated large absorbances attributed to NCO*. Adding water to the feed completely eliminated some of these spectral features and substantially reduced others, providing evidence for isocyanate hydrolysis, as reported by Lesage et al. [8] and Szailer et al. [18]. However, our steady-state experiments included both NO and CO in the gas phase, which makes it difficult to determine if stored NOx could be reduced through an isocyanate intermediate. To answer this question, we collected DRIFTS spectra while cycling the catalyst between lean and rich gas streams. The spectra obtained at 300 °C with 0.9% CO, 5% H_2O, and 5% CO_2 present in the rich phase are shown in Fig. 13. The peak at 2016 cm^{-1} is due to CO on precious metals, and the peak at 2162 cm^{-1} has been identified as NCO* on Ba [8,18]. While the presence of NCO* does not prove that

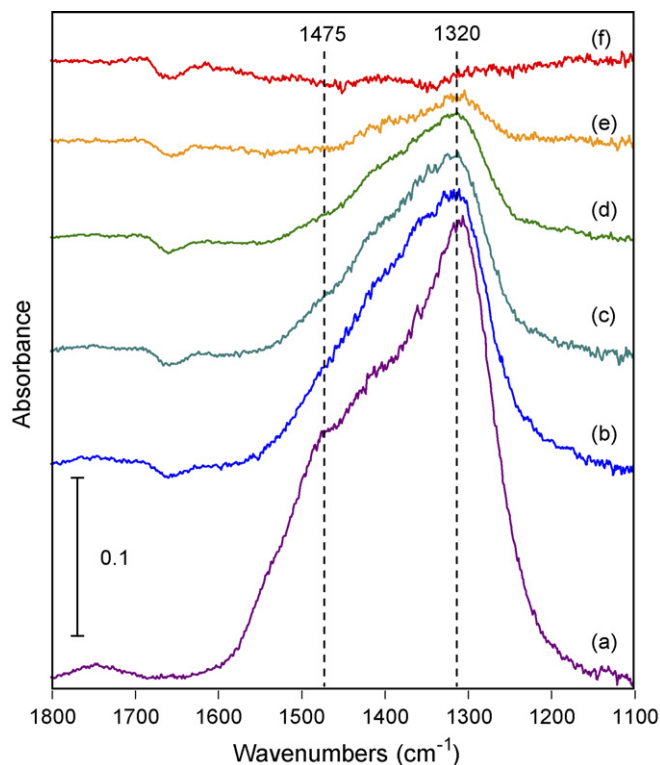Fig. 11. DRIFTS spectra of Umicore GDI LNT wafer at 300 °C exposed to 300 ppm NO/10% O_2/balance Ar for 5 min, 100% Ar for 5 min, and 500 ppm NH_3/balance Ar for (a) 0 min, (b) 2 min, (c) 4 min, (d) 6 min, (e) 8 min, and (f) 10 min.
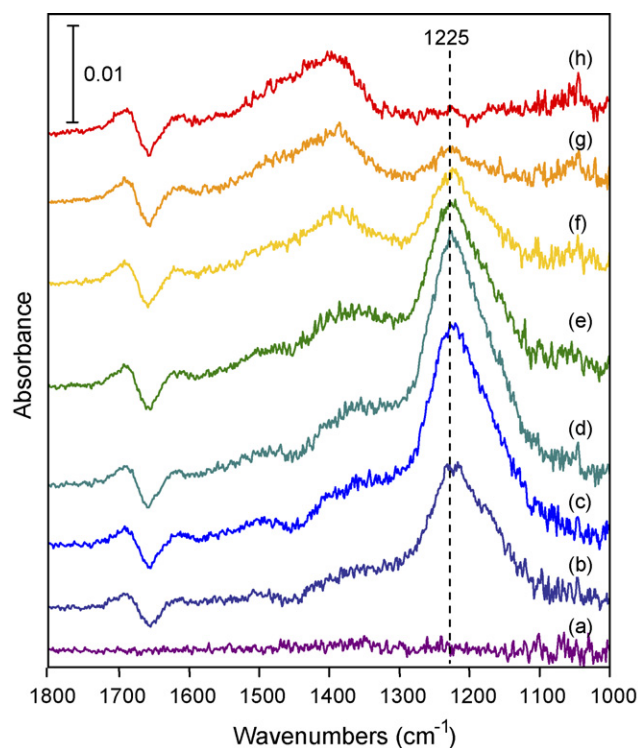

Fig. 12. DRIFTS spectra of Umicore GDI LNT wafer at 300 °C exposed to 10% O_2/balance Ar for 5 min, 100% Ar for 5 min, and 500 ppm NH_3/balance Ar for (a) 0 min, (b) 1 min, (c) 2 min, (d) 3 min, (e) 4 min, (f) 5 min, (g) 6 min, and (h) 7 min.
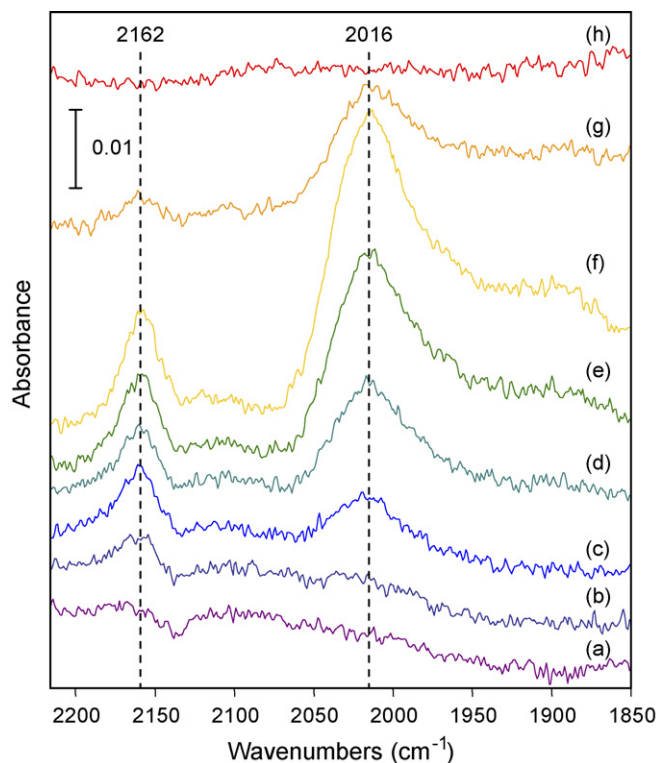
Fig. 13. DRIFTS spectra of Umicore GDI LNT wafer while cycling between 300 ppm NO, 10% O_2, 5% CO_2, 5% H_2O, balance Ar (6.5 min) and 0.9% CO, 5% CO_2, 5% H2O, balance Ar (1 min). Spectra collected (a) 18 s, (b) 24 s, (c) 30 s, (d) 36 s, (e) 42 s, (f) 48 s, (g) 54 s, and (h) 60 s after switching from lean to rich.
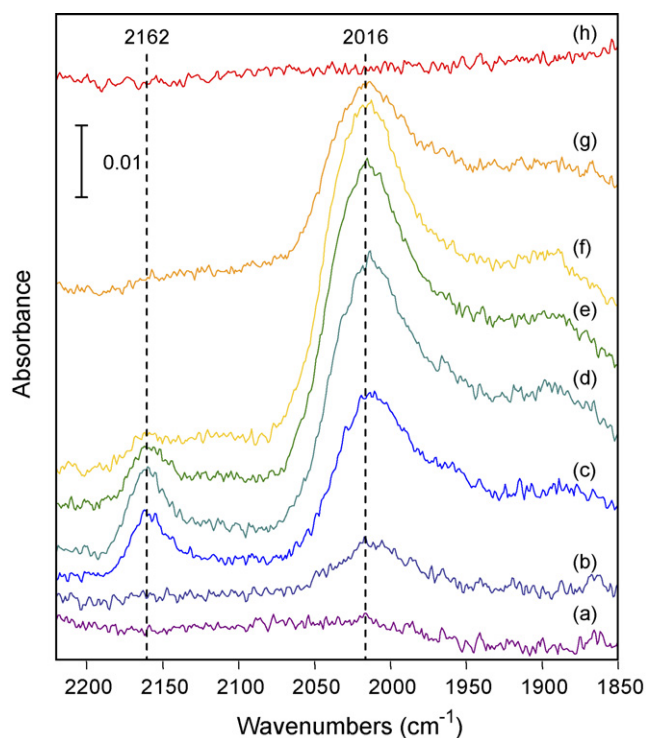

Fig. 14. DRIFTS spectra of Umicore GDI LNT wafer while cycling between 300 ppm NO, 10% O_2, 5% CO_2, 5% H_2O, balance Ar (6.5 min) and 0.9% H_2, 5% CO_2, 5% H_2O, balance Ar (1 min). Spectra collected (a) 18 s, (b) 24 s, (c) 30 s, (d) 36 s, (e) 42 s, (f) 48 s, (g) 54 s, and (h) 60 s after switching from lean to rich.

isocyanate hydrolysis is occurring, it does lend some credibility to the theory. Future experiments will focus on more conclusive evidence for the role of isocyanate.

Fig. 14 shows the DRIFTS spectra for experiments with H_2 instead of CO as the reductant. Interestingly, they look nearly identical to the spectra collected with CO, showing both the CO peak at 2016 cm^{-1} and the NCO peak at 2162 cm^{-1}. This result was somewhat surprising since we had assumed that reaction with adsorbed H* would be the dominant reduction mechanism with H_2 as the reductant. However, this experiment shows that NCO* may still be a reduction intermediate in the presence of CO_2 with H_2 as the reductant.

Taken together, the above DRIFTS experimental results appear to provide important independent support for the proposed kinetic mechanism. Thus, we are encouraged to continue our efforts to combine this mechanism with appropriate NOx storage reactions and thereby produce a transient LNT model capable of simulating all phases of the capture–regeneration cycle.

6. Conclusions

We have developed an elementary surface reaction mechanism describing the chemistry on the precious metal sites of a lean NOx trap. Kinetic parameters for all 28 reactions were found by fitting reactor simulations to an extensive experimental database. The thermodynamic consistency of the mechanism was assured through the imposition of appropriate constraints. The mechanism is able to reproduce quite well the results for 21 separate experimental runs, including the formation and destruction of N_2O and NH_3. Multiple steady-state behavior was observed for a few cases due to the existence of parallel reduction pathways. DRIFTS experiments provided support for key mechanistic steps, including the oxidation of NH_3 by NOx and oxygen species stored on the catalyst surface and the presence of isocyanate during lean/rich cycling. The mechanism reported here is currently being integrated with reactions for NOx storage and release, with the goal of developing a quantitative model capable of predicting product speciation during fully transient operation. We anticipate that the inclusion of mass transfer resistance in both the gas-phase boundary layer and the washcoat may be needed in these simulations.

References

[1] N. Takahashi, H. Shinjoh, T. Iijima, T. Suzuki, K. Yamazaki, K. Yokota, H. Suzuki, N. Miyoshi, S. Matsumoto, T. Tanizawa, T. Tanaka, S. Tateishi, K. Kasahara, Catal. Today 27 (1996) 63.

[2] W.S. Epling, L.E. Campbell, A. Yezerets, N.W. Currier, J.E. Parks, Catal. Rev. 46 (2004) 163.

[3] S. Poulston, R.R. Rajaram, Catal. Today 81 (2003) 603.

[4] P. Jozsa, E. Jobson, M. Larsson, Top. Catal. 30–31 (2004) 177.

[5] H. Abdulhamid, E. Fridell, M. Skoglundh, Top. Catal. 30–31 (2004) 161.

[6] L. Olsson, E. Fridell, M. Skoglundh, B. Andersson, Catal. Today 72 (2002) 263.

[7] L. Lietti, P. Forzatti, I. Nova, E. Tronconi, J. Catal. 204 (2001) 175.

[8] T. Lesage, C. Verrier, P. Bazin, J. Saussey, M. Daturi, Phys. Chem. Chem. Phys. 5 (2003) 4435.

[9] T. Lesage, C. Verrier, P. Bazin, J. Saussey, S. Malo, C. Hedouin, G. Blanchard, M. Daturi, Top. Catal. 30–31 (2004) 31.

[10] L. Castoldi, I. Nova, L. Lietti, P. Forzatti, Catal. Today 96 (2004) 43.

[11] J.E. Parks, S. Huff, J.A. Pihl, J.-S. Choi, B. West, SAE Technical Paper Series, 2005-01-3876, 2005.

[12] J.A. Pihl, J.E. Parks, C.S. Daw, T.W. Root, SAE 2006 Trans. J. Engines, 2006-01-3441, 2006.

[13] I. Nova, L. Lietti, L. Castoldi, E. Tronconi, P. Forzatti, J. Catal. 239 (2006) 244.

[14] W.S. Epling, A. Yezerets, N.W. Currier, Appl. Catal. B 74 (2007) 117.

[15] K.S. Kabin, R.L. Muncrief, M.P. Harold, Catal. Today 96 (2004) 79.

[16] I. Nova, L. Castoldi, L. Lietti, E. Tronconi, P. Forzatti, Top. Catal. 42–43 (2007) 21.

[17] L. Cumaranatunge, S.S. Mulla, A. Yezerets, N.W. Currier, W.N. Delgass, F.H. Ribeiro, J. Catal. 246 (2007) 29.

[18] T. Szailer, J.H. Kwak, D.H. Kim, J.C. Hanson, C.H.F. Peden, J. Szanyi, J. Catal. 239 (2006) 51.

[19] R.S. Larson, V.K. Chakravarthy, J.A. Pihl, C.S. Daw, SAE Technical Paper Series, 2006-01-3446, 2006.

[20] J. Xu, R. Clayton, V. Balakotaiah, M.P. Harold, Appl. Catal. B 77 (2008) 395–408.

[21] W.S. Epling, A. Yezerets, N.W. Currier, Catal. Lett. 110 (2006) 143.

[22] J.A. Pihl, M.S. Thesis, University of Wisconsin-Madison, 2005.

[23] T.J. Toops, D.B. Smith, W.P. Partridge, Appl. Catal. B 58 (2005) 245.

[24] G.L. Powell, M. Milosevic, J. Lucania, N.J. Harrick, Appl. Spectrosc. 46 (1992) 111.

[25] J. Sirita, S. Phanichphant, F.C. Meunier, Anal. Chem. 79 (2007) 3912.

[26] R.J. Kee, F.M. Rupley, J.A. Miller, M.E. Coltrin, J.F. Grcar, E. Meeks, H.K. Moffat, A.E. Lutz, G. Dixon-Lewis, M.D. Smooke, J. Warnatz, G.H. Evans, R.S. Larson, R.E. Mitchell, L.R. Petzold, W.C. Reynolds, M. Caracotsios, W.E. Stewart, P. Glarborg, CHEMKIN Collection, Release 3.5, Reaction Design Inc., San Diego, CA, 1999.

[27] J.D. Griffin, T.G. Kolda, R.M. Lewis, Sandia National Laboratories Report SAND2006-4621, 2006.

[28] J.H.B.J. Hoebink, R.A. van Gemert, J.A.A. van den Tillaart, G.B. Marin, Chem. Eng. Sci. 55 (2000) 1573.

[29] E. Fridell, A. Rosen, B. Kasemo, Langmuir 10 (1994) 699.

[30] L. Olsson, H. Persson, E. Fridell, M. Skoglundh, B. Andersson, J. Phys. Chem. B 105 (2001) 6895.

[31] W.C. Hecker, A.T. Bell, J. Catal. 92 (1985) 247.

[32] R. Burch, J.P. Breen, F.C. Meunier, Appl. Catal. B 39 (2002) 283.

[33] W.C. Hecker, A.T. Bell, J. Catal. 85 (1984) 389.

[34] R.D. Hawthorn, AIChE Symp. Ser. No. 137, 70 (1974) 428.

[35] A. Holmgren, B. Andersson, Chem. Eng. Sci. 53 (1998) 2285.

[36] M. Uberoi, C.J. Pereira, Ind. Eng. Chem. Res. 35 (1996) 113.

[37] K. Chakravarthy, C.S. Daw, J.C. Conklin, SAE Trans. 111 (2002) 876.

[38] M. Caracotsios, W.E. Stewart, Comput. Chem. Eng. 9 (1985) 359.

[39] C. Sedlmair, K. Seshan, A. Jentys, J.A. Lercher, J. Catal. 214 (2003) 308.